IOP Publishing and International Atomic Energy Agency Nuclear Fusion
Nucl. Fusion **52** (2012) 123009 (9pp) doi:10.1088/0029-5515/52/12/123009

Two-dimensional characterization of ELM precursors in NSTX

Y. Sechrest[1], T. Munsat[1], D.J. Battaglia[2] and S.J. Zweben[2]

[1] Department of Physics, University of Colorado, Boulder, CO 80309, USA
[2] Princeton Plasma Physics Laboratory, Princeton, NJ 08540, USA

Received 30 July 2012, accepted for publication 11 October 2012
Published 6 November 2012
Online at stacks.iop.org/NF/52/123009

Abstract
Gas puff imaging has been used to capture the two-dimensional evolution of edge-localized mode (ELM) precursors. Precursor events were observed preceding ELMs and ELM-induced H–L back-transitions in radio-frequency heated H-mode plasmas, and the growth of the precursor mode through the ELM filamentation was imaged in the plane perpendicular to the local B-field. Strong edge intensity modulations appeared to propagate in the electron diamagnetic direction while steadily drifting radially outwards. Intensity fluctuations were observed at frequencies around 20 kHz and wavenumbers of 0.05–0.2 cm^{-1}. Upon growing to a trigger point, precursor fluctuations were seen to form filamentary structures and move into the scrape-off layer (SOL) explosively with radial velocities peaking at 8 km s^{-1}. Once in the SOL, filaments reverse their propagation direction and travel in the ion diamagnetic direction. Edge intensity fluctuations are strongly correlated with magnetic signals from Mirnov coils, and toroidally distributed coils estimated toroidal mode numbers of $n = 5$–10. Quantitatively similar precursors have been observed in ohmic H-mode plasmas as well, though significantly fewer events are seen in the ohmic cases and none were observed in the near-threshold NBI H-modes studied.

(Some figures may appear in colour only in the online journal)

1. Introduction

The achievement of a high confinement mode, or H-mode, in ITER is widely considered necessary to reach the operational goals of the project: namely, a burning plasma with a ratio of fusion power generated to input power of 10 [1, 2]. The improved confinement in H-mode operation is partly attributed to the development of an edge transport barrier (ETB) that restricts the transport of particles and heat into the scrape-off layer (SOL), thus reducing losses to the wall along open field lines [3]. The ETB then builds up a region of steep gradients in temperature and density near the plasma edge known as the H-mode pedestal. These steep gradients provide a source of free energy for a number of disruptive instabilities known as edge-localized modes, or ELMs [4]. ELMs are often explosive events that eject significant energy into the SOL; upon contacting the plasma-facing components, these energy bursts can exceed the heat load limits of the material components and cause significant damage. Current projections predict that ITER components will not be able to tolerate the impulsive energy densities of the largest ELM events [5]. Therefore, it is clear that a thorough understanding of ELM physics and a strategy for avoiding and/or mitigating ELMs is necessary for next-step fusion devices to succeed.

Our understanding of the physical and operational aspects of ELMs has seen much progress in the last two decades (see [4, 6] for general reviews and [7–10] for reviews of recent work). Currently, the most widely accepted view is that ELMs are triggered by ideal MHD modes driven unstable by edge pressure gradients and edge current profiles [7, 11]. In particular, the theory of peeling–ballooning modes has been successful in describing observed stability boundaries [12–14] for large type-I ELMs, though the nonlinear growth of the modes and the dynamics of the crash are not well understood theoretically.

In recent years, the development of fast edge diagnostics has produced detailed descriptions of the full ELM cycle including ELM filament structure [15–17] and precursor modes have been identified in nearly all major tokamak experiments. Precursor modes have been observed in density fluctuations from reflectometry measurements, electron temperature fluctuations from electron cyclotron emission measurements, and magnetic signals (e.g. [18, 19]). Type-I ELM precursors are often found in the frequency range 5–25 kHz, and they are observable up to 200–500 μs preceding the ELM event. Typically these modes exhibit low to intermediate toroidal mode numbers of $n = 2$–20. One-dimensional imaging systems viewing visible light fluctuations in the plasma edge have also been used to observe ELM fine-structure on ASDEX [20] and ELM precursors on Alcator C-MOD [21], and two-dimensional imaging systems have been used on MAST to examine ELM filament structure

[22, 23]. How the precursor modes participate in the ELM crash, however, is still unclear.

Observations performed on the National Spherical Torus Experiment (NSTX) [24] have observed precursor modes in magnetic signals or ultra-soft x-ray data in each of three distinct ELM classes: large (type-I), medium and small (type-V). Large ELMs were preceded by a rapidly growing precursor mode observed on Mirnov coil arrays, and typical toroidal mode numbers for the mode were $n = 5$–8. Medium ELMs were usually preceded by a long-lived $n = 1$ mode visible on ultra-soft x-ray diagnostics, and small ELMs had a short-lived $n = 1$ magnetic precursor. In addition, ELM filament structure has been examined using GPI observations in several ELMing regimes [25, 26], and measurements of NBI heated H-modes with type-III ELMs captured the birth of filamentary structures in two dimensions over $\sim$50 μs [25]. However, coherent ELM precursors were not observed in the imaging data.

In this paper, we present results from two-dimensional imaging of precursor modes preceding small ELM events in NSTX. Gas puff imaging (GPI) of visible light fluctuations near the last closed flux surface has revealed precursor edge intensity fluctuations that are wave like in nature. These edge oscillations are seen to grow in amplitude preceding ELM events and H–L back-transitions, but they are also observed intermittently at low amplitudes throughout H-mode operation. A magnetic signature is also observed that is concurrent and strongly correlated with the edge intensity oscillations. The nonlinear evolution of the precursor mode and ELM crash have been imaged in the plane perpendicular to the magnetic field using the GPI diagnostic, and the two-dimensional structure and dynamics are analysed and presented here. Precursor modes were imaged primarily in near-threshold RF-heated H-modes and some ohmic heated cases, but they were absent in the similar, near-threshold NBI heated cases studied.

This work provides a detailed characterization of the precursor fluctuations and the dynamics leading to the ELM crash. Section 2 outlines the experimental details of the observations including a brief description of the GPI diagnostic. Analysis of the precursor begins with the presentation of GPI observations in section 3, which is followed by time-frequency analysis of the precursor in section 4. Magnetic fluctuations are discussed in 5, and the paper concludes with a discussion of results (section 6) and a brief summary (section 7).

2. Experimental details

The experimental observations discussed in this paper were obtained on the low aspect ratio NSTX (major radius $R = 0.86$ m, minor radius $a = 0.67$ m) at the Princeton Plasma Physics Laboratory [27]. Each discharge is a deuterium plasma with an on-axis toroidal field $B_t = 0.45$ T and a plasma current $I_p = 900$ kA. Table 1 contains specific details for each shot, and example traces of I_p, radio-frequency power P_{RF}, and D_α light for a single shot are shown in figure 1.

This collection of shots was originally designed to probe the RF power threshold for the low to high-confinement mode transition in NSTX. The RF heating system used is a 12 antenna high harmonic fast wave (HHFW) heating system that can deliver up to 6 MW of power at 30 MHz [28]. The database of

Table 1. Shot database for this study including the shot number, time frame of interest, toroidal magnetic field, plasma current and RF heating power.

Shot #	Time frame (s)	B_T (T)	I_P (kA)	P_{RF} (kW)
141917	0.23–0.25	0.45	900	625
141917	0.25–0.27	0.45	900	1200
141918	0.22–0.24	0.45	900	625
141919	0.23–0.25	0.45	900	625
141920	0.24–0.25	0.45	900	625
141922	0.24–0.27	0.45	900	700
142000	0.22–0.25	0.45	900	1100
142001	0.22–0.25	0.45	900	1100
142002	0.22–0.25	0.45	900	1100
142003	0.22–0.25	0.45	900	1100
142006	0.25–0.27	0.45	900	1100

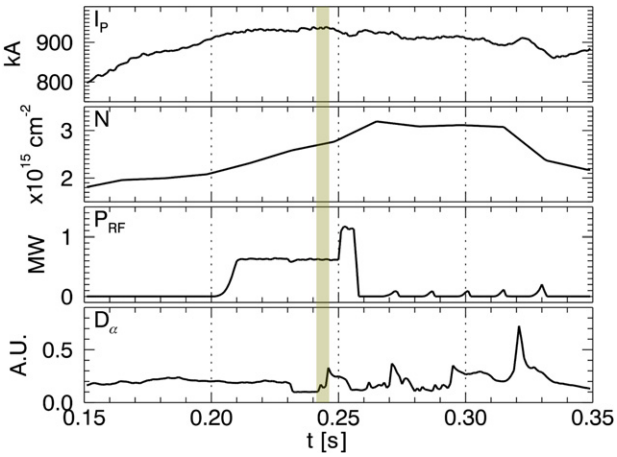

Figure 1. Time traces of RF heating power P_{RF}, plasma current I_P, D_α light and line-integrated density N for shot 141919 from this study. Neutral beams are also used early in the shot for plasma conditioning. The shaded region indicates the time period for traces plotted in figure 3.

shots considered in this study are RF-heated H-mode plasmas with 0.5–1.2 MW of input RF heating power operated at 180° phasing to optimize core heating efficiency [29, 30].

The classification of ELM type is not straightforward in this operational regime. Low heating powers suggest that type-III ELMs would be most likely; however, a distinguishable ELM frequency is not observed. Additionally, the presence of L–H–L dithers further complicates identification. Alternatively, ELM precursors observed in this regime are most similar to precursors observed in type-I ELMing regimes on NSTX, namely, precursors are short-lived and exhibit intermediate toroidal mode numbers. Regardless of ELM type, the events studied here are small, and the stored energy drop in most events is below the measurable limit. However, the stored energy is observed to drop 3–5% during events which trigger H–L transition.

The primary observations used in this work are from the GPI diagnostic, which images visible light fluctuations in the edge region of the plasma. For this method of imaging, a gas manifold, positioned at the wall of the device and above the outboard midplane, emits a neutral gas puff into the edge region of the plasma. Spectral line emission from the collisionally excited atoms is collected by a fibre optic bundle that views the plasma through a reentrant port at the wall of the device.

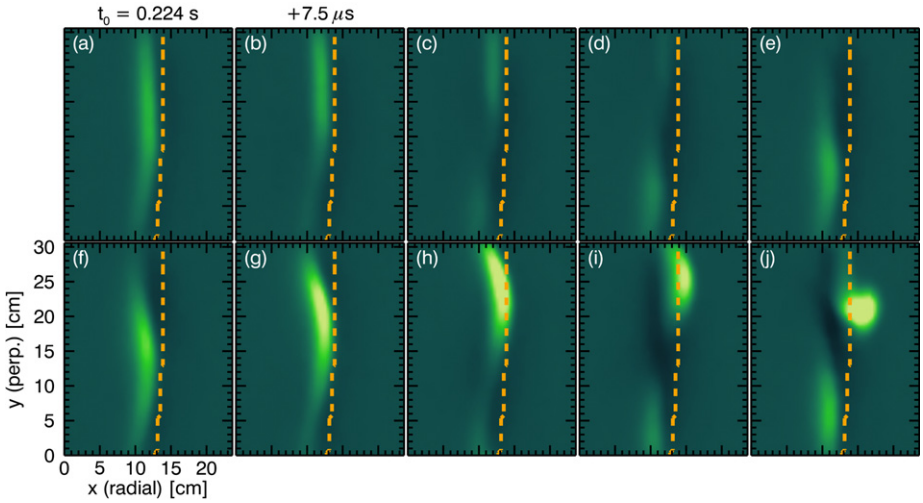

Figure 2. Multiframe image stills of an ELM event with precursor intensity fluctuations from shot 141918. The time between frames is ~7.5 μs. Distinct mode structure can be seen in precursor oscillations leading to the ejection of the filament in the last two frames. The approximate location of the separatrix is indicated by the dashed line.

The light captured by the fibre bundle is filtered and imaged by a Phantom v710 fast-framing camera at 400 000 frames per second (2.5 μs per frame). For the current work, deuterium is used for the neutral gas species, and D_α (656 nm) line emission is imaged using optical filters. Further details on the GPI diagnostic and the physics of the visible light fluctuations have been presented previously [31, 32].

The diagnostic viewing direction is set to be nearly field aligned at the intersection of the view with the gas puff, thus cross sections of field-aligned structures can be localized by the visible light emitted from the gas puff. In this study, image dimensions are 64 × 80 pixels, and the view is roughly 25 cm × 30 cm. The view is aligned such that the horizontal (x) direction of the camera image is approximately codirectional with the radial direction, and the vertical (y) direction is then perpendicular to both the magnetic field and the radial direction. Therefore, the vertical direction is approximately the projection of the poloidal direction into the plane perpendicular to the magnetic field. Herein, we refer to the horizontal direction as *radial* and the vertical as *perpendicular*.

3. Coherent edge intensity oscillations

We have analysed GPI measurements from the shots listed in table 1 and have identified a periodic edge intensity fluctuation seen to precede ELMs and ELM-induced H–L back-transitions during RF-heated H-mode operation. These edge oscillations have a distinct, elongated mode structure and are visible up to 200 μs preceding the ELM event. While these fluctuations are seen to precede ELM events, low-amplitude oscillations are also seen intermittently throughout RF H-mode operation. In this section, we detail the GPI observations of the ELM precursors.

A series of image stills from the GPI diagnostic is displayed in figure 2 to illustrate the general features of the precursor phase leading to the ELM crash. Edge intensity oscillations with a distinct elongated structure are visible preceding the ejection of plasma captured in frames (i)–(j). During the precursor phase, frames (a)–(h), intensity peaks travel in the positive y direction (in the electron diamagnetic direction), and as one peak leaves the camera view a second peak enters from the bottom. The intensity structures appear to drift radially outwards and become increasingly deformed as they propagate through the camera view. This deformation is especially evident in frame (h) directly preceding the filamentation. Eventually, an unidentified process is triggered precipitating the explosive ejection of plasma filaments into the SOL. Once in the SOL, the filaments travel in the reverse direction (-y, ion diamagnetic direction). This reversal of the propagation direction is commonly attributed to a change in the radial electric field from inside to outside the separatrix. In many observed ELM events clear filamentation is evident such as in figure 2(j). However, the ELM crash is a complicated nonlinear process, thus the ejection of plasma into the SOL does not always follow the clear time evolution shown in figure 2.

From the GPI image sequence, we can define two quantities which will be of use in the following analysis. The first of these is the integrated edge intensity I_{edge}, which is defined here as the sum of the intensity ±2 cm around the radial location of the peak time-averaged intensity profile. The second quantity is the ratio of light in the SOL to the images total intensity, F_{SOL}. This quantity is a measure of the relative intensity in the SOL, thus it is a good indicator of plasma loss into the SOL such as ELM events, intermittent blobs and turbulent losses during L-mode operation. During an H–L transition the mean value of F_{sol} can change by 0.15–0.20, while ELMs can cause deviations greater than 0.40 for a large event. The precursor oscillations are easily observable in time traces of either of these quantities as seen in figure 3. I_{edge} fluctuations preceding an ELM event can be seen at 0.2427 s, and an ELM-induced H–L transition is triggered at 0.245 s. Low level periodic fluctuations can be seen near 0.244 s as well. These intermittent, low-amplitude fluctuations are found throughout RF H-mode operation, and are similar in frequency and wavenumber to the precursor oscillations, as will be discussed in the following section.

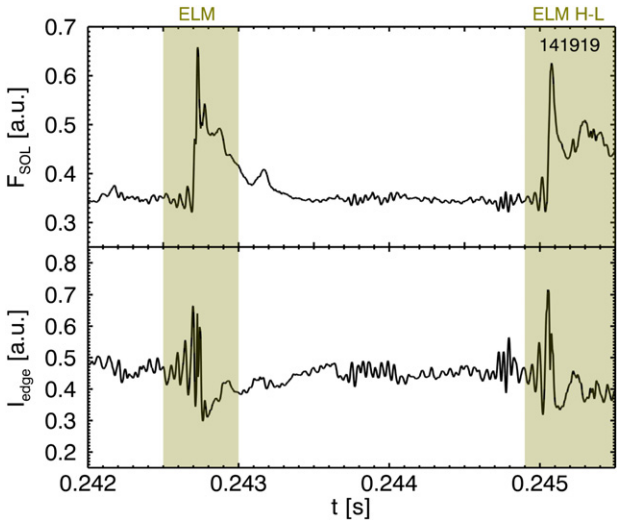

Figure 3. Time traces of (*a*) SOL fraction F_{SOL} and (*b*) integrated edge intensity I_{edge} corresponding to the shaded time period in figure 1. Traces show edge intensity fluctuations preceding an ELM at 0.2425 s, and an ELM-induced back-transition at 0.245 s. Low level fluctuations can also be seen near 0.244 s.

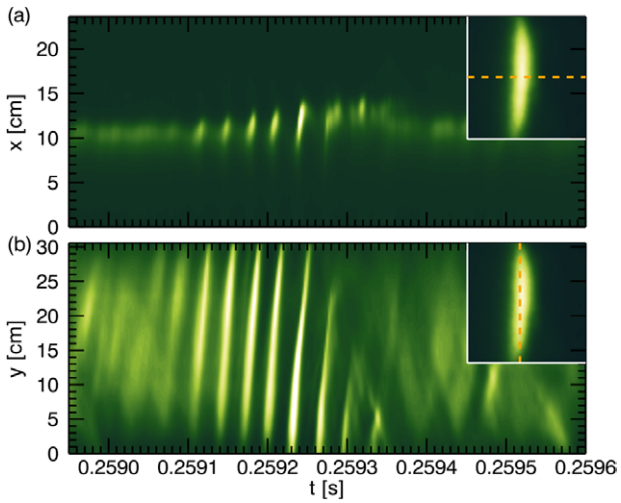

Figure 4. Two-dimensional slices through GPI data from shot 141918 with one cut at $y = 15.5$ cm (*a*) and one at $x = 10.5$ cm (*b*). Precursor fluctuations are very distinct brightness pulses which appear to move upwards, or in the electron diamagnetic direction indicated by the tilt of structures in (*b*). Structures are also seen to drift radially outwards as indicated by $+x$ motion in (*a*).

Figure 4 illustrates the coherent nature of the precursor oscillations. The figure shows two-dimensional 'slices' of the GPI data with (*a*) one cut in x (radial) versus time at $y = 15.50$ cm and (*b*) one cut in y (perpendicular) versus time at $x = 10.5$ cm. The fluctuating intensity pattern is easily discernible in (*a*) at time 0.2592 s, and the intensity peaks appear to drift radially outwards as the mode grows. A similar pattern is evident in (*b*) where the tilt in the intensity pattern, typically referred to as streaks, indicates propagation in the positive y (electron diamagnetic direction). A simple linear fit to the intensity streaks gives an estimate of the perpendicular velocity of $\sim$13 km s^{-1}.

For a more refined velocity estimate, we employ digital image velocimetry based on pattern-matching techniques [33]

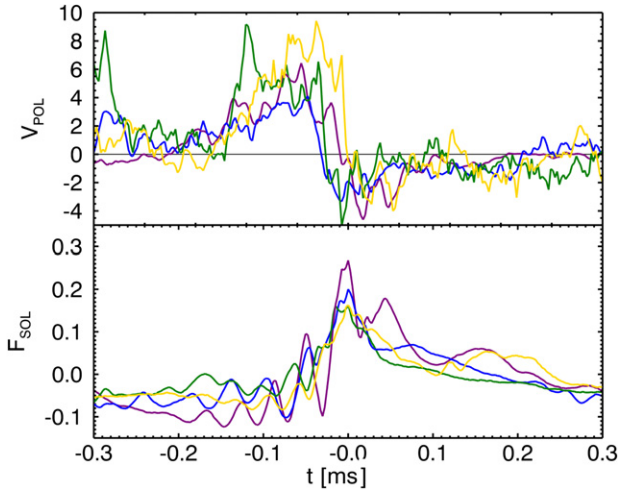

Figure 5. Traces of (*a*) average perpendicular velocities and (*b*) F_{SOL} for many ELM events from the shots database. Velocities are measured $\sim$2 cm inside the separatrix. Timings are relative to the peak F_{SOL} for each event.

to estimate the two-dimensional flow field of the precursor intensity fluctuations. Perpendicular velocities averaged in the vertical direction and measured just inside the separatrix are plotted in figure 5 along with F_{SOL} traces. The figure shows the flow behaviour during several observed ELM events with precursor fluctuations. Times for figure 5 are relative to the peak in F_{SOL}, so that the ejection of plasma occurs near $t = 0.0$ ms and precursor activity can be seen between -0.2 and 0.0 ms. Average perpendicular velocities measured inside the separatrix during the precursor period typically range between +2–8 km s^{-1}, but velocity estimates measured at the intensity maximum are in agreement with the streak fit estimates. At the time of the ELM crash, measured radial velocities of intensity structures can peak as high as 8 km s^{-1} as filaments are ejected into the SOL. Additionally, average perpendicular velocities measured inside the separatrix are seen to briefly reverse direction during the crash, and reach flows up to -4 km s^{-1}.

During the evolution of the precursor the edge intensity profile becomes deformed, and portions of the intesnity profile balloon into the SOL as they propagate through the GPI view. The radial excursion of the intensity fluctuations and the ballooning-like deformation are both observable in figures 2(*a*)–(*g*). To quantify these features of the mode, we first define the plasma edge, $x_{\mathrm{edge}}(y)$ by taking a weighted average of the x coordinate at each y location using the cube of the intensity as the weight for each point. This weighting ensures that the edge location closely follows the peak of the radial profile of the intensity, and this yields a definition for the 'edge' which is consistent with a visual estimate. When turbulence fluctuations are low, such as in H-mode, the GPI neutral gas puff penetrates an approximately poloidally uniform distance in from the plasma edge, so that x_{edge}, to a rough approximation, traces out a flux surface. Thus we will consider perturbations of x_{edge} to be a proxy for perturbations of the outer flux surface. Figures 6(*a*)–(*b*) illustrate an example of x_{edge}. The edge curvature and maximum radial excursion may then be derived from x_{edge}.

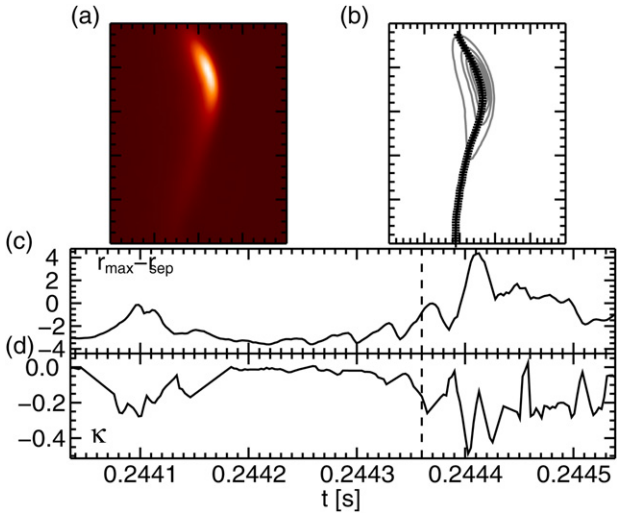

Figure 6. Example (*a*) image frame from shot 141917 and (*b*) x_{edge} function overlayed on intensity contours. Maximum radial excursion relative to EFIT separatrix location is plotted in (*c*), and the edge curvature, κ corresponding to this point is plotted in (*d*). The dashed line indicates the time point of image (*a*).

The maximum radial excursion at any given time corresponds to the right-most point, or point with largest x value, on the x_{edge} curve, and the time evolution of this position relative to the EFIT separatrix is plotted in figure 6(*c*). The EFIT separatrix location is typically uncertain to ± 1 cm at the location of the GPI view, and MHD activity generally associated with ELMs will perturb the location of the separatrix. Additionally, the EFIT time resolution for this analysis is 4 ms, but over a 0.1 s period during H-mode the reconstructed position of the separatrix is slowly varying and changes by no more than 3 cm. So, we believe it to be a reasonable estimate of the equilibrium separatrix location about which the fast time-scale behaviour fluctuates. Furthermore, it is the most physically meaningful reference location available, so we choose to use it for relative measurements of the radial position of the edge. It should be noted that the choice of reference does not significantly change any of the conclusions.

The curvature of the edge is calculated using the mathematical definition: $\kappa = x''/(1 + x'^2)^{3/2}$, and the necessary derivates are calculated from a quintic spline fit of x_{edge} using two internal knots. In this work, negative curvature indicates that the convex side is directed radially outwards. Figure 6(*d*) shows a time trace of the curvature measured at the point of maximum radial excursion for that time point.

Precursor activity can be observed in figures 6(*c*) and (*d*) between 0.2442 and 0.2444 s, and modulations of the radial excursion and the edge curvature are evident. These modulations coincide with intensity peaks passing through the camera view as seen in figure 2. As the precursor mode evolves, the radial excursion increases, and the curvature becomes increasingly negative indicating significant deformation of the edge. Briefly following the image in 6(*a*), a filament forms and is explosively ejected into the SOL near $t = 0.2444$ s. After this time, a well-defined edge does not exist until the turbulence is quenched.

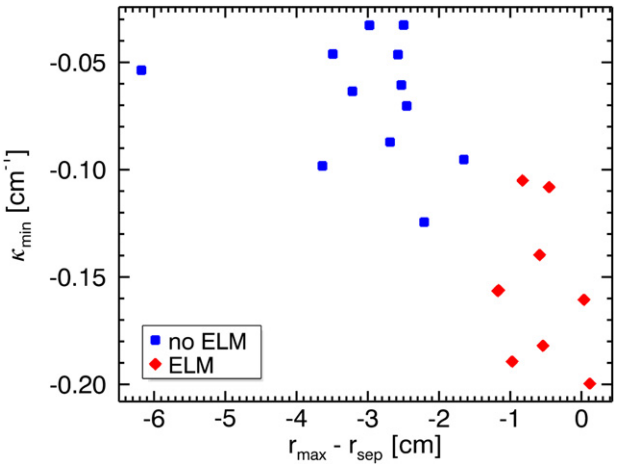

Figure 7. Scatterplot of minimum edge curvature, κ_{min} and maximum radial excursion relative to the EFIT separatrix location for several ELM precursor events (diamonds). Intensity fluctuations not leading to an ELM are also included (squares).

Several precursor events are compared in figure 7, and low-amplitude events (such as in figure 3 at 0.2440) that do not precipitate an ELM are also included. The figure compares the minimum (i.e. most negative) curvature κ_{min} and the maximum radial excursion during each event. Events directly preceding ELMs are found to reach closer to the EFIT separatrix location, and curvature values for these events are more negative than events not preceding ELMs. Therefore, the curvature appears to be an important characteristic of the underlying instability, and the increased curvature for ELM unstable events suggests that this mode participates in the ELM event. Still, it is unclear why the mode sometimes saturates at a low amplitude, and does not always precipitate an ELM.

4. Wavenumber-frequency analysis

Time-frequency analysis of the integrated edge intensity I_{edge} is performed using the continuous wavelet transform (CWT) [34]. This method is similar to the familiar technique of windowed Fourier transforms; however, the CWT uses a 'mother' wavelet function that is scaled and translated to measure the power contained in a signal at a given location in time-scale (frequency) space, thus one obtains a time-frequency power spectrum analogous to the spectrogram of windowed Fourier transforms. The advantage of the CWT is the inherent ability of the scaling operation to yield an optimal product of the time and frequency resolutions at each frequency value. The variable resolution allows the CWT to capture the fine details of a signal near singularities while still providing efficient measurement of lower-frequency behaviour.

The 6th order Morlet CWT of the I_{edge} signal from figure 3 is presented in figure 8 along with the accompanying F_{SOL} trace. The ELM and H–L back-transition events are directly preceded by significant increases in power in the 20–30 kHz band, and the low-amplitude oscillations between 0.243 and 0.244 s also show significant levels of power near 25 kHz. Other shots in this collection exhibit similar activity in the 20–30 kHz range, both preceding ELM events and at low levels intermittently throughout H-mode operation. Power increases

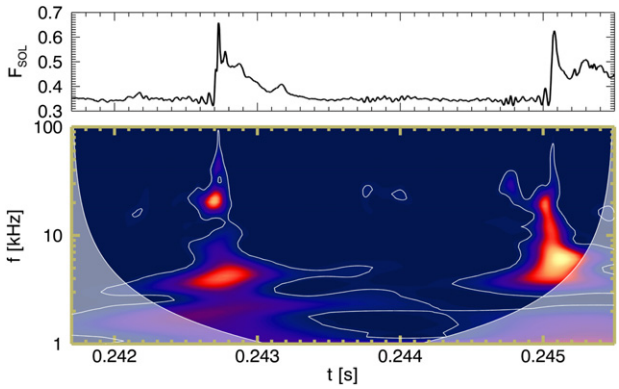

Figure 8. Wavelet scalogram of integrated edge intensity, I_{edge} accompanied by the time trace of the SOL fraction for shot 141919. The power spectrum shows significant power at the 20 kHz scale during the ELM precursor fluctuations. The shaded region in the wavelet scalogram indicates where edge effects become important, and the white contour indicates the 95% significance level.

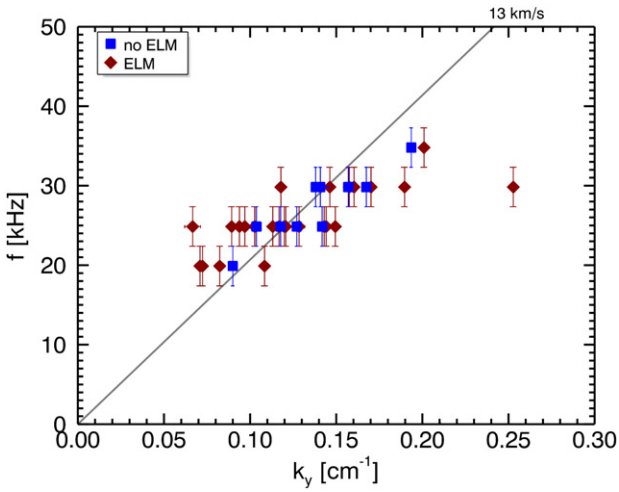

Figure 9. Scatter plot of frequency of precursor fluctuations against the perpendicular wavenumber derived from GPI intensity fluctuations. Red triangles are events that lead to an ELM or back-transition, while blue squares are edge intensity fluctuations that do not lead to an ELM.

in the 3 kHz range are associated with the time-scale of the full ELM event including the period of increased fluctuations following the crash.

Short time window FFT analysis has also been used to corroborate the results of the CWT analysis, and cross-spectral analysis of intensity fluctuations at locations distributed in the vertical direction provides an estimate of perpendicular wavenumbers, k_y for the precursor. Several short time periods from the shots listed in table 1 which exhibit periodic edge intensity fluctuations have been analysed, and the results are presented in figure 9. In agreement with the CWT analysis, typical frequencies are in the range 20–30 kHz, and perpendicular wavenumbers are found to be between 0.05 and 0.21 cm^{-1}. Periods preceding ELM events and periods of low-amplitude fluctuations were both analysed and no significant difference in wavenumber or frequency was found between the two sets of events. Additionally, the points cluster about a phase velocity of $\sim$13 $km\,s^{-1}$, which is consistent with the image velocimetry estimates. In this case, the pattern-

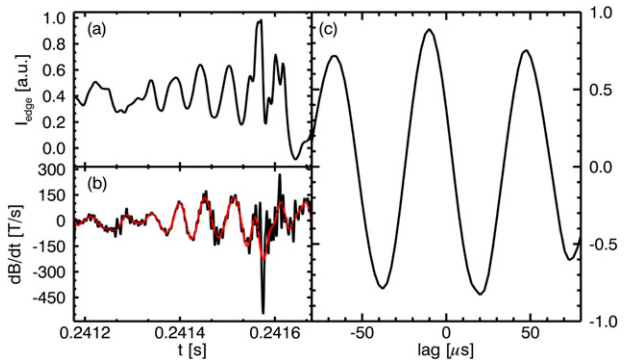

Figure 10. Time traces of (*a*) I_{edge} and (*b*) low-pass filtered magnetic signals from shot 141917. The black trace has been low-pass filtered at 200 kHz, and the red trace has been bandpass filtered around 20 kHz. Magnetic traces are strongly correlated with fluctuations in edge intensity as shown in the lagged correlation plot (*c*). Absolute values of the correlation coefficient reach 0.8 for periods during the precursor activity.

matching velocimetry is tracking the motion of individual intensity peaks and troughs because of the size of the wave relative to the size of the search pattern. Therefore, it is expected that the velocimetry estimate would be consistent with the phase velocity.

5. Magnetic fluctuations

Signals from magnetic pick-up coils distributed in toroidal angle around the device have also been analysed, and precursor activity in the 20 kHz region is observed in the time derivative of the magnetic field ($\dot{B}$). Time traces of I_{edge} and a low-pass filtered $\dot{B}$ signal are plotted in figures 10(*a*) and (*b*), respectively. These traces illustrate the similarities in the precursor behaviour, and indeed the $\dot{B}$ signal filtered below 200 kHz and the I_{edge} signal are highly correlated as shown in figure 10(*c*). The figure shows the time-lagged correlations for 200 μs long time segments preceding the ELM crash, and the coil with the highest correlation is chosen for figures 10(*b*) and (*c*). This particular coil is separated 30° in toroidal angle from the GPI view, and is located below the midplane. Additionally, this coil is located near field lines that pass through the GPI view. The absolute value of the correlation coefficient exceeds 0.8 at -10 μs, thus the magnetic fluctuations measured at this position are delayed with respect to the intensity fluctuations. The high correlation suggests that the precursor edge intensity fluctuations seen by GPI are electromagnetic in nature as one would expect for typical MHD instabilities believed to produce ELMs.

Toroidal mode numbers are estimated from a toroidally distributed array of magnetic pick-up coils. Time traces of $\dot{B}$ 0.3 ms in length and directly preceding ELM events are Fourier transformed, and precursor modes are identified as peaks in the power spectrum. Toroidal mode numbers are then determined from the phase of the precursor Fourier mode as a function of toroidal position of the magnetic coil. This simple method assumes a global mode, and it does not account for the possibility of a frequency modulation during the mode evolution. We find that toroidal mode numbers between $n = 5$–10 are typical for precursor behaviour similar to what

has been plotted in figure 10. For comparison, it is possible to estimate toroidal mode numbers from the perpendicular wavenumbers estimated from the GPI data. If the structures are assumed to be aligned with the magnetic field, then the perpendicular wavelength can be mapped to an equivalent toroidal wavelength given the magnetic pitch angle. Using this mapping, toroidal mode number estimates from imaging are between $n = 4$–15 which agrees with the magnetic coil estimate.

6. Discussion

The previous sections have characterized a particular ELM precursor observed by the GPI diagnostic as well as magnetic diagnostics. In this section, we discuss the interpretation of the dynamics of the precursor, and its involvement in the ejection of plasma from the closed flux region. In addition to these points, the edge plasma conditions for precursor activity and the connection with possible instabilities is discussed.

6.1. Precursor mode evolution

Several similarities exist between ELM filaments and transport due to turbulence-born coherent structures or blobs (see recent review [35] and references therein). In both field-aligned coherent structure—a blob, or a filament in the case of an ELM—forms that propagates radially outwards. Both blobs and ELMs are thought to arise because of a nonlinear saturation mechanism. However, blobs are typically local disturbances that emerge from the background turbulence, while ELMs are correlated with the growth of global MHD instabilities. In contrast to typical blob-driven scenarios, the ELM precursors discussed in this paper exhibit long wavelength, coherent oscillations seen both in imaging and Mirnov coil signals. Furthermore, the precursors have several spatially distributed intensity peaks that contribute to the ELM event. These structures can be seen in the SOL following the crash as they pass through the camera view travelling in the -y direction. For these reasons, the precursor description appears to be more accurate than the blob description for the events studied here. However, it is likely that the interactions between the turbulence (including blobs), the transport barrier and MHD instabilities all contribute to the ELM event.

The evolution of the precursor mode through the ELM crash is of particular interest, and an important question to ask is: what role does the precursor play in triggering an ELM? In figure 9, it was found that low-amplitude fluctuations were indistinguishable in frequency and wavenumber from precursor fluctuations, so the precursor fluctuations could be uncorrelated with the ELM event. However, there are several counterpoints to this argument. Firstly, when the fluctuations are present and an ELM occurs, the fluctuations (both intensity and $\dot{B}$) are seen to grow exponentially preceding the crash. Secondly, the imaging gives us several clear examples (e.g. figure 2) where a particular intensity wave crest is directly involved in the ELM crash, and the wave crest can be tracked as it is ejected into the SOL. Finally, figure 7 indicates that the deformation of the edge due to the fluctuations (evident in figure 2) is a distinguishing feature of events that become unstable to an ELM. This picture suggests that the precursor plays some role in the ELM crash, though illuminating the physical process by which the precursor participates in the crash is difficult. One noteworthy point, however, is that the deformation of the edge is qualitatively similar to disturbances due to ballooning-like or peeling instabilities [36]. Therefore, this feature may be indicative of an instability driven by edge pressure or currents. Still, an ELM event is a complicated nonlinear process likely involving the interaction of several physical processes.

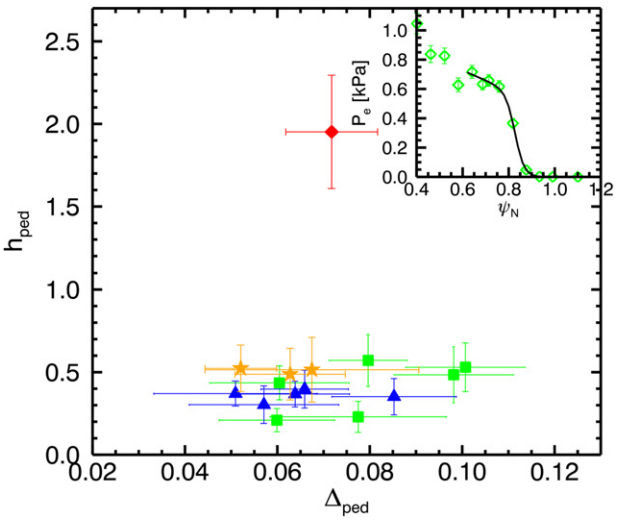

Figure 11. Pedestal parameters for height h_{ped} and width Δ_{ped} are extracted from a modified tanh fit to the electron pressure profile (inset) and a comparison of several shots is presented. Squares are 0.6–1.0 MW RF shots, triangles are ohmic H-mode shots, stars are $\sim$ 1.0 MW NBI shots, and the diamond is a 4 MW NBI heated shot.

6.2. Edge plasma conditions and stability

ELMs are believed to be a result of MHD instabilities driven by the edge pressure gradient and edge currents, and one of the most successful models for ELMs is the peeling–ballooning model [12, 14]. In this model, pressure driven ballooning modes couple to current driven peeling modes at finite toroidal mode numbers, thus intermediate mode numbers are predicted to be the most unstable modes. This model has been used in numerical simulations, and has been successful in describing observed type-I ELM stability boundaries in a number of machines [13, 14].

In accord with peeling–ballooning predictions, the precursor modes studied here exhibit intermediate toroidal mode numbers, and a full edge stability analysis could possibly provide a positive identification for the driving instability. However, the ELM events in this study did not occur with a consistent frequency, and, due to variations in applied heating, pressure profiles typically evolved continuously throughout each shot. Therefore, pressure profiles and gradients could not be adequately constrained for edge stability simulations.

In light of these difficulties, we seek insight into the stability through characterizing the electron pressure profiles and edge pressure gradients. Figure 11 shows a typical edge electron pressure profile for the near-threshold RF-heated plasmas, and a modified tanh fit [37, 38] to the data. Here, ψ_n

is a normalized flux coordinate defined as

$$\psi_n = \frac{\psi_c - \psi}{\psi_c - \psi_s},$$

where ψ_c is the flux at the core and ψ_s is the flux at the separatrix. Pedestal width Δ_{ped} and pedestal height h_{ped} are parameters of the fit function, and a comparison of these parameters for different shots is included in figure 11. Parameter uncertainties are estimated by manually varying one parameter about the best fit, and then performing a reduced fit with that parameter fixed. The error bars indicate the variation in the parameter that yields a change in the reduced χ^2 of the fit of $\Delta\chi^2 = 1$.

The comparison illustrated by figure 11 indicates that ohmic H-modes (triangles) have similar edge electron pressure profiles as the near-threshold RF H-modes (squares). In fact, ELM precursors quantitatively similar to those observed in RF heated plasmas were observed in several ohmic H-mode discharges. However, 34 events with the precursor magnetic signature were observed in the nine RF shots analysed, while only six events were observed in eight ohmic shots. Pedestal characteristics of low-power NBI heated shots were also similar to the ohmic and RF-heated cases within the uncertainties, and GPI data from 3 NBI heated shots near L–H threshold power were analysed for precursor behaviour. Additionally, 10 NBI heated shots in the type-I ELMing regime were analysed, but no short-lived coherent precursors were observed in the GPI data for any of the NBI heated shots. Although a detailed discussion of the high-power NBI shots is beyond the scope of this paper, it is worth noting that in these cases GPI may not observe far enough into the plasma to identify precursor modes due to the physics of the neutral gas puff. To improve this comparison, more GPI data from near-threshold NBI heated plasma discharges is needed; however, we will discuss the available data below with a focus on the near-threshold shots.

The prevalence of the precursor in the RF cases suggests that RF effects—such as increased impurity content, fast-ion populations and changes in the flow profile—may increase the drive of underlying instabilities for the precursor, thus increasing their occurrence. Alternatively, these effects could slow the growth of these instabilities and extend the precursor lifetime, thus allowing the precursor to be detected. Sputtering from the RF antenna can lead to increased impurity content in the edge, thus cooling the plasma by radiation losses. This cooling could then alter the pressure profile or change the edge stability. Additionally, fast-ions have been suggested to have an impact on the pedestal width [39]. However, our rather limited comparison in figure 11 does not find a significant difference in the pedestal parameters of the electron pressure between heating methods. It should be noted that we are limited to considering only the electron pressure in this study because neutral beams required for charge exchange recombination spectroscopy (CXRS) were absent in most cases. Also, this collection of shots was chosen to have similar plasma conditions and heating power levels, but these shots were not specifically engineered to test the difference in heating methods. A recent study on JET [40] has examined the differences between neutral beam and ion cyclotron heating in ELMy H-mode scenarios, and it was found that pedestal width and height are independent of the heating method in this regime.

One of the main differences between the neutral beam heating and the other heating methods, RF and ohmic, is the momentum input by neutral beams leading to a toroidal spin-up of the plasma. Therefore, one might ask if toroidal flow shear accounts for the lack of precursor behaviour observed in the NBI shots analysed here. Unfortunately, as previously mentioned, the RF cases do not have access to toroidal flow measurements from CXRS. Numerical studies [41, 42], however, predict flow shear to be stabilizing for short wavelengths and destabilizing for long wavelengths, though the overall effect on the stability limit is typically small [41]. The absence of short-lived, coherent precursors in the available GPI data of NBI heated cases remains unresolved, and exists as a topic for future exploration.

7. Summary

GPI measurements made during RF-heated H-mode plasmas have observed wave-like edge intensity ELM precursors. The full two-dimensional dynamics of the growth of the precursor mode, the filamentation and the crash were captured and presented here. Strong edge intensity modulations were observed propagating in the electron diamagnetic direction with average perpendicular velocities of $\sim$8 km s^{-1} preceding ELM events. Intensity fluctuations appeared at frequencies near 20 kHz with perpendicular wavenumbers between 0.05 and 0.2 cm^{-1}. Precursor modes modulated the radial position of the edge and the edge curvature as well, and ELM unstable edge oscillations were found to have more negative curvature values than ELM stable events. These intensity fluctuations also appear to be electromagnetic in nature as they were strongly correlated with magnetic pick-up coil data. Furthermore, intermediate toroidal mode numbers of $n = 5$–10 have been estimated from the magnetic data.

Precursors were observed in GPI data of both RF-heated and ohmically heated H-modes, but were not present in the NBI heated discharges studied here. Additionally, electron pressure profiles for shots with and without precursor activity were examined, and pedestal widths and heights for the two populations were found to be similar. Unfortunately, pressure profiles could not be adequately constrained for edge stability simulations, and a complete stability analysis is left to future work.

ELMs will continue to be a concern for next-step fusion devices, and a complete understanding of the phenomenon and strategies to mitigate or suppress them will be required. In this paper, we have presented a detailed characterization of the evolution of the ELM precursor through the ELM crash, and toroidal mode number estimates for precursors were found to be consistent with peeling–ballooning predictions. Additionally, the nonlinear evolution of the mode has been captured in two-dimensions, and it is hoped that these observations can provide points of comparison for numerical studies.

Acknowledgments

Work supported by the US Department of Energy under grant DE-SC0001966 and DE-FG02-08ER54995. The authors

would also like to thank A. Diallo, E. Fredrickson, R. Maqueda, S. Sabbagh, T. Osborne and the NSTX team for their support.

References

[1] Shimada M. 2007 Progress in the ITER Physics Basis Chapter 1: Overview and summary *Nucl. Fusion* **47** S1

[2] Wade M.R. 2009 Physics and engineering issues associated with edge localized mode control in ITER *Fusion Eng. Des.* **84** 178–85

[3] Gohil P. 2006 Edge transport barriers in magnetic fusion plasmas *C. R. Physique* **7** 606–21

[4] Zohm H. 1996 Edge localized modes (ELMS) *Plasma Phys. Control. Fusion* **38** 105–28

[5] Zhitlukhin A. *et al* 2007 Effects of ELMS on ITER divertor armour materials *J. Nucl. Mater.* **363** 301–7

[6] Suttrop W. 2000 The physics of large and small edge localized modes *Plasma Phys. Control. Fusion* **42** A1–14

[7] Becoulet M. *et al* and JET-EFDA Workprogramme 2003 Edge localized mode physics and operational aspects in tokamaks *Plasma Phys. Control. Fusion* **45** A93–113

[8] Oyama N. 2008 Progress and issues in understanding the physics of ELM dynamics, ELM mitigation and ELM control *J. Phys.: Conf. Ser.* **123** 012002

[9] Maggi C.F. 2010 Progress in understanding the physics of the H-mode pedestal and ELM dynamics *Nucl. Fusion* **50** 066001

[10] Kamiya K. *et al* 2007 Edge localized modes: recent experimental findings and related issues *Plasma Phys. Control. Fusion* **49** S43–62

[11] Wilson H.R., Cowley S.C., Kirk A. and Snyder P.B. 2006 Magneto-hydrodynamic stability of the H-mode transport barrier as a model for edge localized modes: an overview *Plasma Phys. Control. Fusion* **48** A71–84

[12] Connor J.W., Hastie R.J., Wilson H.R. and Miller R.L. 1998 Magnetohydrodynamic stability of tokamak edge plasmas *Phys. Plasmas* **5** 2687–700

[13] Snyder P.B., Wilson H.R., Ferron J.R., Lao L.L., Leonard A.W., Mossessian D., Murakami M., Osborne T.H., Turnbull A.D. and Xu X.Q. 2004 ELMS and constraints on the H-mode pedestal: peeling–ballooning stability calculation and comparison with experiment *Nucl. Fusion* **44** 320–8

[14] Snyder P.B., Wilson H.R., Ferron J.R., Lao L.L., Leonard A.W., Osborne T.H., Turnbull A.D., Mossessian D., Murakami M. and Xu X.Q. 2002 Edge localized modes and the pedestal: a model based on coupled peeling–ballooning modes *Phys. Plasmas* **9** 2037–43

[15] Oyama N., Asakura N., Chankin A.V., Oikawa T., Sugihara M., Takenaga H., Itami K., Miura Y., Kamada Y., Shinohara K. and JT-60 Team 2004 Fast dynamics of type I ELMS and transport of the ELM pulse in JT-60U *Nucl. Fusion* **44** 582–92

[16] Neuhauser J. *et al* and ASDEX Upgrade Team 2008 Structure and dynamics of spontaneous and induced ELMS on ASDEX Upgrade *Nucl. Fusion* **48** 045005

[17] Leonard A.W. *et al* and Pedestal Edge Physics ITPA Topical Group 2006 Survey of type I ELM dynamics measurements *Plasma Phys. Control. Fusion* **48** A149–62

[18] Oyama N., Shinohara K., Kamada Y., Miura Y., Oikawa T. and Takeji S. 2001 *Plasma Phys. Control. Fusion* **43** 717–26

[19] Perez C.P. *et al* and JET-EFDA Contributors 2004 *Nucl. Fusion* **44** 609

[20] Endler M., Garcia-Cortes I., Hidalgo C., Matthews G.F., ASDEX Team and JET Team 2005 The fine structure of ELMs in the scrape-off layer *Plasma Phys. Control. Fusion* **47** 219–40

[21] Terry J.L., Cziegler I., Hubbard A.E., Snipes J.A., Hughes J.W., Greenwald M.J., LaBombard B., Lin Y., Phillips P. and Wukitch S. 2007 The dynamics and structure of edge-localized-modes in Alcator C-Mod *J. Nucl. Mater.* **363** 994–9

[22] Kirk A., Wilson H.R., Counsell G.F., Akers R., Arends E., Cowley S.C., Dowling J., Lloyd B., Price M., Walsh M. and MAST Team 2004 Spatial and temporal structure of edge-localized modes *Phys. Rev. Lett.* **92** 245002

[23] Kirk A., Koch B., Scannell R., Wilson H.R., Counsell G., Dowling J., Herrmann A., Martin R., Walsh M. and MAST Team 2006 Evolution of filament structures during edge-localized modes in the MAST tokamak *Phys. Rev. Lett.* **96** 185001

[24] Maingi R. *et al* 2005 H-mode pedestal, ELM and power threshold studies in NSTX *Nucl. Fusion* **45** 1066–77

[25] Maqueda R.J., Maingi R. and NSTX Team 2009 Primary edge localize mode filament structure in the national spherical torus experiment *Phys. Plasmas* **16** 056117

[26] Maingi R., Hubbard A.E., Meyer H., Hughes J.W., Kirk A., Maqueda R., Terry J.L., Alcator C-Mod Team, MAST Team and NSTX Team 2011 Comparison of small ELM characteristics and regimes in Alcator C-Mod, MAST and NSTX *Nucl. Fusion* **51** 063036

[27] Kaye S.M. *et al* and NSTX Team 2001 Initial physics results from the national spherical torus experiment *Phys. Plasmas* **8** 1977–87

[28] Ryan P.M. *et al* 2001 Initial operation of the nstx phased array for launching high harmonic fast waves *Fuison Eng. Des.* **56–57** 569–73

[29] Hosea J. *et al* and NSTX Team 2008 High harmonic fast wave heating efficiency enhancement and current drive at longer wavelength on the National Spherical Torus Experiment *Phys. Plasmas* **15** 056104

[30] Taylor G. *et al* 2010 Advances in high-harmonic fast wave physics in the National Spherical Torus Experiment *Phys. Plasmas* **17** 056114

[31] Maqueda R.J., Wurden G.A., Zweben S., Roquemore L., Kugel H., Johnson D., Kaye S., Sabbagh S. and Maingi R. 2001 Edge turbulence measurements in NSTX by gas puff imaging *Rev. Sci. Instrum.* **72** 931–4

[32] Zweben S.J. *et al* and NSTX Team 2004 *Nucl. Fusion* **44** 134

[33] Munsat T. and Zweben S.J. 2006 *Rev. Sci. Instrum.* **77** 103501

[34] Torrence C. and Compo G.P.1998 A practical guide to wavelet analysis *Bull. Am. Meteorol. Soc.* **79** 61–78

[35] D'Ippolito D.A., Myra J.R. and Zweben S.J. 2011 Convective transport by intermittent blob-filaments: comparison of theory and experiment *Phys. Plasmas* **18** 060501

[36] The ASDEX Team 1989 The H-mode of ASDEX *Nucl. Fusion* **29** 1959–2040

[37] Groebner R.J. and Osborne T.H. 1998 Scaling studies of the high mode pedestal *Phys. Plasmas* **5** 1800–6

[38] Diallo A., Maingi R., Kubota S., Sontag A., Osborne T., Podesta M., Bell R.E., LeBlanc B.P., Menard J. and Sabbagh S. 2011 *Nucl. Fusion* **51** 103031

[39] Parail V.V., Guo H.Y. and Lingertat J. 1999 Fast particles and the edge transport barrier *Nucl. Fusion* **39** 369–72

[40] Versloot T.W. *et al* 2011 and JET EFDA Contributors Comparison between dominant NB and dominant IC heated ELMy H-mode discharges in JET *Nucl. Fusion* **51** 103033

[41] Snyder P.B. *et al* 2007 Stability and dynamics of the edge pedestal in the low collisionality regime: physics mechanisms for steady-state ELM-free operation *Nucl. Fusion* **47** 961–8

[42] Aiba N., Tokuda S., Furukawa M., Oyama N. and Ozeki T. 2009 Effects of a sheared toroidal rotation on the stability boundary of the MHD modes in the tokamak edge pedestal *Nucl. Fusion* **49** 065015